We are IntechOpen,
the world's leading publisher of
Open Access books
Built by scientists, for scientists

6,900
Open access books available

186,000
International authors and editors

200M
Downloads

154
Countries delivered to

Our authors are among the

TOP 1%
most cited scientists

12.2%
Contributors from top 500 universities

CLARIVATE ANALYTICS
BOOK CITATION INDEX
INDEXED

WEB OF SCIENCE™

Selection of our books indexed in the Book Citation Index
in Web of Science™ Core Collection (BKCI)

Interested in publishing with us?
Contact book.department@intechopen.com

Characterization of Defects Evolution in Bulk SiC by Synchrotron X-Ray Imaging

T. S. Argunova, M. Yu. Gutkin, J. H. Je,
V. G. Kohn and E. N. Mokhov

Additional information is available at the end of the chapter

1. Introduction

Optimization of Silicon Carbide (SiC) bulk growth by physical vapor transport (PVT) has allowed commercial realization of SiC wafers with low defect density. Dislocated micropipes (MPs), known as the most killing defects in SiC devices, have been reduced to the density levels as low as 0.7–0.5 cm^{-2}. However applications of SiC as a material for high-power electronics are still hampered. High-performance high-power electric systems require SiC devices capable of handling the current capacity of at least 100 A, which means that the MP density of SiC wafer should be less than 0.5 cm^{-2} [16]. Fabrication of such high quality wafers, in particular, in low cost is indispensable for manufacturing of high-current devices.

Various methods such as the enhancement of polytype stability [26, 31], the reduction of screw dislocations [22], the restriction of inclusions [23], *etc.*, help control MP density. Polytype transformation, dislocations, and MPs, and their interaction or conversion are complicated phenomena which are of particular interest to SiC crystal growers and device engineers. Dislocations are largely induced by foreign polytype inclusions (FPIs) [27], but disappear when the inclusions transform back to the initial polytype [26]. The improvement of the polytype stability immediately and dramatically decreases the MP densities [29]. When accumulated at the boundaries of FPIs, MPs may coalesce each other, forming pores [10, 11, 13].

Nowadays, dislocation processes in SiC single crystals are studied by means of Synchrotron Radiation (SR) X-ray topography [24, 25, 33] combined with defect selective etching [30] or computer simulation of Bragg-diffraction images [3, 18]. A very good methodology to study hollow defects in SiC — to map them and to evaluate their sizes — is phase contrast X-ray imaging [19], which is available due to high spatial coherency of third generation SR sources.
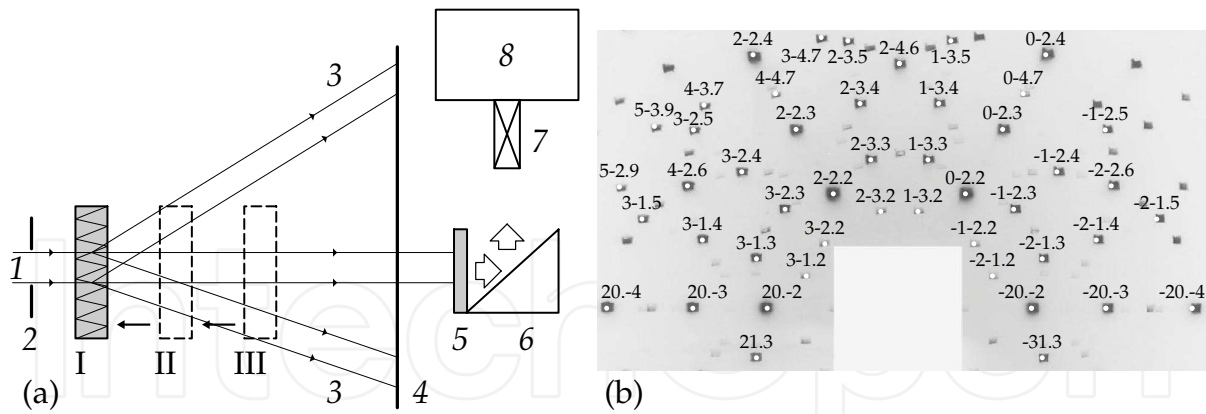
Figure 1. (a) Scheme for obtaining diffraction and phase-contrast images on-line: (*1*) SR beam from storage ring, (*2*) beam defining slits, (*3*) diffracted beams, (*4*) film, (*5*) mirror, (*6*) scintillator, (*7*) objective, (*8*) detector. I, II and III correspond to the succession of 6*H*-SiC axial-cut slices investigated in turn. (b) Laue pattern of the (0001) 6*H*-SiC wafer (direction [1$\bar{2}$10] horizontal) fixed perpendicular to SR beam.

The purpose of the present paper is to characterize the evolution of pores and MPs during SiC growth using SR white beam phase contrast imaging and Bragg diffraction topography. We document defect reduction mechanisms and suggest theoretical and computer models to explain them.

2. Experimental

The samples used in this study were prepared from a 4*H* and 6*H*-SiC boules grown in Ar by the sublimation sandwich technique [31]. The Ar pressure in the growth chamber was 80 mbar. The growth temperature was 2180°C, and the growth rate was 0.5 mm $\times$ h^{-1}. The crystals were N-doped and had a *n*-type conductivity with a donor concentration 2×10^{18} cm^{-3}. They contained B to a concentration $(1–2) \times 10^{17}$ cm^{-3}. Besides, doping of SiC by Al to a concentration of approximately $(2–7) \times 10^{17}$ cm^{-3} occurred because of the Al presence in the polycrystalline SiC source. After polished and treated to eliminate damaged layers on both sides, the sample thicknesses were controlled as about 500 μm.

The foreign polytype inclusions located close to the surface were revealed with the aid of a photoluminescence (PL) microscope in visible as well as in ultraviolet light under the magnifications of $50\times$ – $200\times$. The polytype was identified by the color of PL [28]. The opening of pores and MPs on molten KOH etched sample surfaces was detected using optical and scanning electron microscopies (SEM), performed with Zeiss universal microscope and JEOL JSM-6330F FESEM, respectively.

Imaging experiments were done at the 7B2 X-ray microscopy beamline of Pohang Light Source (PLS), Korea [2]. The 7B2 bending magnet port of the PLS storage ring provided an effective source size of the order of 60 μm (160 μm) in the vertical (horizontal) direction at the distance 34 m from the sample. Unmonochromatized ('white') radiation with the spectrum ranged from 6 to 40 keV was propagated through a polished beryllium window of 2 mm thick and then through a specimen with no optical elements in between.

X-ray phase contrast in the white beam is formed because of a small angular size and a high spatial coherence of third generation SR source. The white beam spectrum has a curve shape with a maximum at a certain energy in the case at hand. Decreases in the radiation intensity at high and low energies are caused by the SR generation's nature and the absorption in the

sample, respectively. Therefore, even 'white' SR is partially coherent, which is quite sufficient for recording phase-contrast images of small objects such as MPs in SiC [19].

White rather than monochromatic beam gives higher intensity, larger exposed area, the use of various research methods during a single experiment, but has the attendant disadvantage that obtained information is mostly qualitative. The task of obtaining reliable information can be solved by developing numerical simulation of phase-contrast images. Such an approach was recently proposed [1, 19] based on Kirchhoff integral calculation for monochromatic SR harmonics followed by summation over an actual spectrum, taking into account the absorption in sample. In particular, the Fit Microtube Image (FIMTIM) program was developed for automatic determination of the parameters of the MP cross section in two dimensions from the good-fit condition for calculated and experimental profiles of relative intensity. From this it was shown that MP cross section can vary not only in its size, but also in its orientation, during its growth [1].

In our studies, MPs are assumed to be screw dislocations with hollow cores [17], as made certain by combining phase contrast imaging and topography. Evolution of pores and MPs during SiC growth presents a substantial challenge, because a SiC boule is not transparent as a whole even for hard synchrotron X-rays. The series of slices were cut perpendicular (on-axis) and parallel (axial-cut) to the growth direction of $6H$ and $4H$-SiC boules. Between on-axis $6H$-SiC slices, the shapes and distributions of defects were variable. It was essential to have some special means of finding the same area of interest between the slices. Taking into account the microscopic sizes of defects, this area was controlled as rather small as 1.5 mm $\times$ 1.5 mm. X-ray phase-contrast micro-imaging was utilized for the area mapping, and the Laue pattern served for orientation.

Fig. 1(a) shows the experimental set-up combining phase contrast imaging and topography techniques. In a diffraction mode, topographs were recorded on a photographic film. Phase-contrast images were taken with a charge coupled device camera (14-bit gray scale and 1600 $\times$ 1200 pixels range). Before recorded X-ray image was converted into visible lights by a 150 μm thick CdWO$_4$ scintillator and magnified by a lens system with a magnification from 1$\times$ to 50$\times$.

Six on-axis $6H$-SiC wafers were numbered as 'wafer I' (adjacent to the seed), 'wafer II' (the next to grow), and so the last wafer near the top of the boule as 'wafer VI'. The area mapping was preceded by the following orientation procedure. Each wafer was mounted with a miscut line, that is, an intersection between the surface and the basal plane (0001), vertical and the surface perpendicular to the beam. Each wafer was aligned to have the same Laue pattern of the orientation. For instance, the wafers I, II, III in the succession of one to another are sketched on Fig. 1(a). Fig. 1(b) shows an indexed Laue pattern for the (0001) orientation obtained from the wafer I at a distance of 9 cm. Similar patterns were then recorded from the wafer II, and so on.

3. The evolution of defects during SiC growth

Defect evolution from wafer to wafer was investigated on the area of interest from the matched overlap of the wafer images. For example, Fig. 2(a) shows the matched overlap of the wafer I (gray) cut off near the seed and the next wafer II (black). The region 1 is the area of interest, while the region 2 is a reference point to refine the wafer match. Here a group of MPs undeviatingly propagated through all the wafers, as demonstrated in Fig. 2(b). Pores and MPs in the region of interest 1 in the wafers I and II are displayed in Figs. 2(c) and (d),
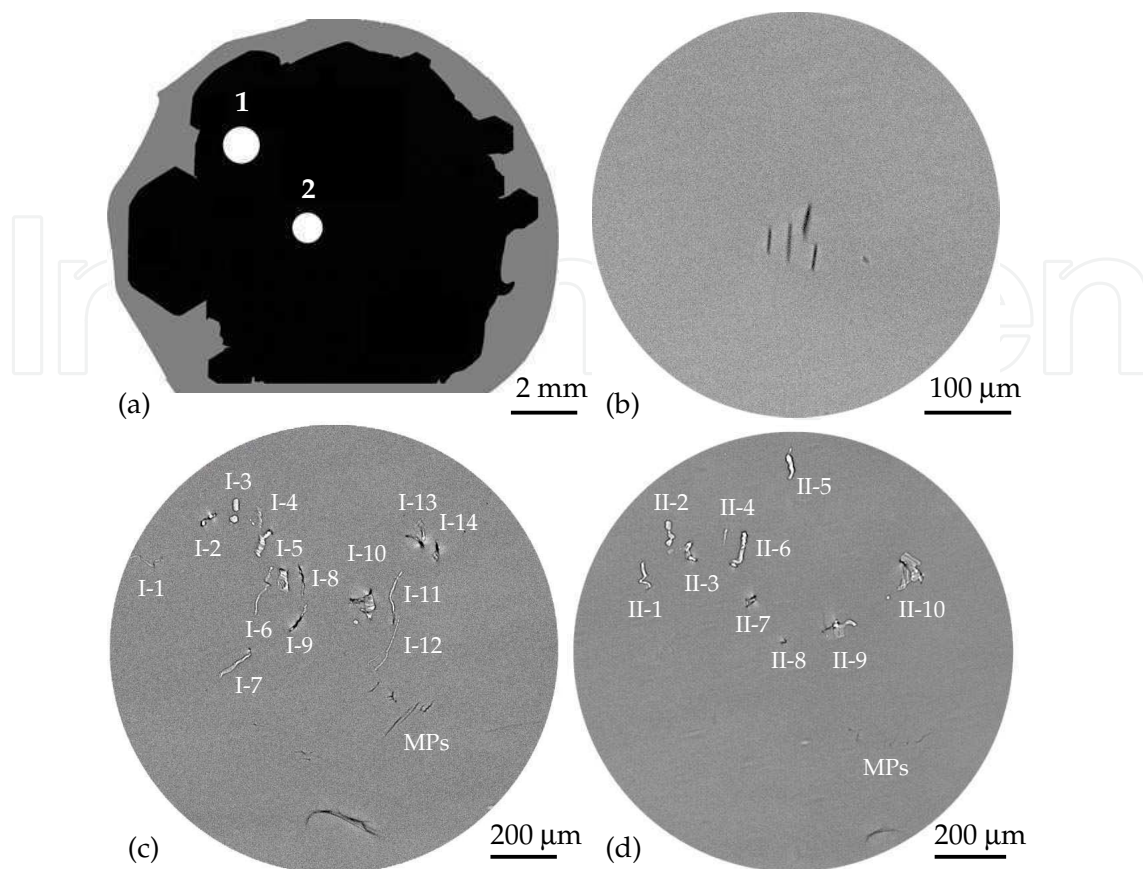
Figure 2. (a) The outline of the wafers I (gray) and II (black) imaged after the Laue pattern adjustment is completed. The area 1 is the area of interest. The wafer images are lapped over in such a way that the positions of propagating MPs encircled by the area 2 overlie in SR phase contrast images of (b). Comparison of SR phase contrast images of pores in the wafers I (c) and II (d).
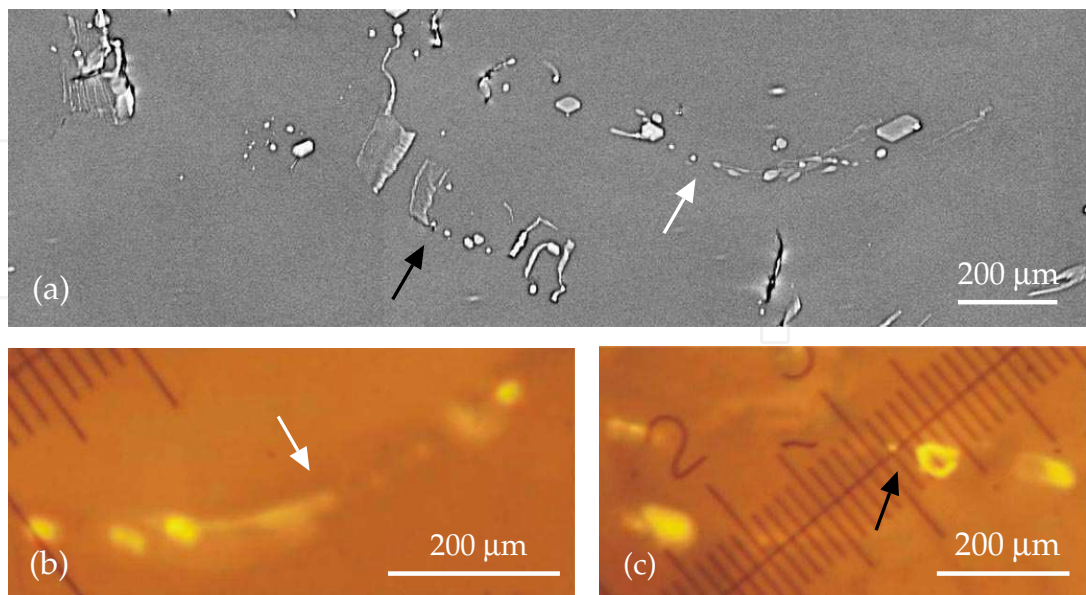

Figure 3. (a) SR phase-contrast image of the pores in the wafer I. (b) PL micrographs of 4*H*-SiC inclusions in 6*H*-SiC matrix; the white in (b) and the black in (c) arrows point to the boundaries of the inclusions where the pores are located in (a).
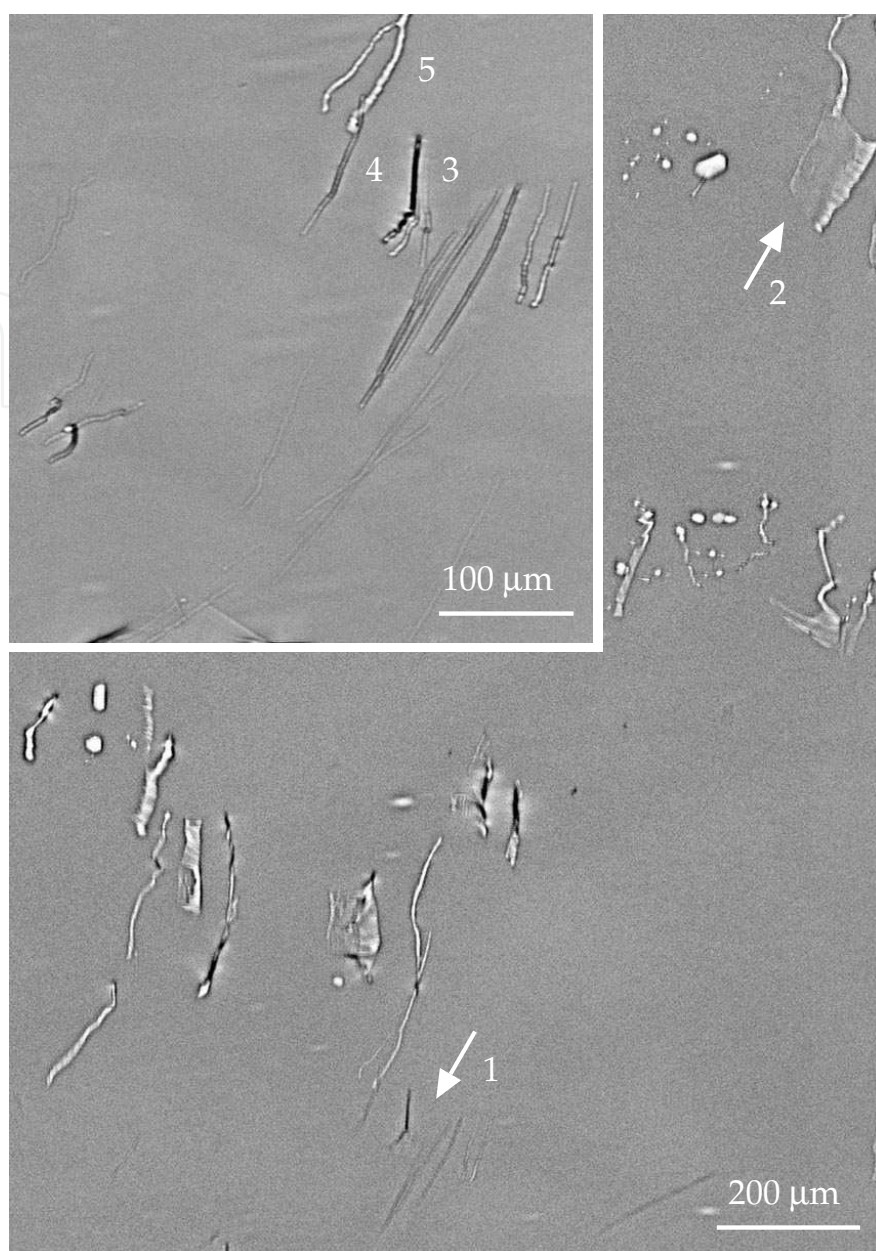
Figure 4. SR phase contrast image of the pores and MPs in the wafer I. The arrows point to the group of MPs (*1*) and the pore (*2*). The group of MPs is magnified in the inset: (*3, 4*) — MPs, (*5*) — pore.
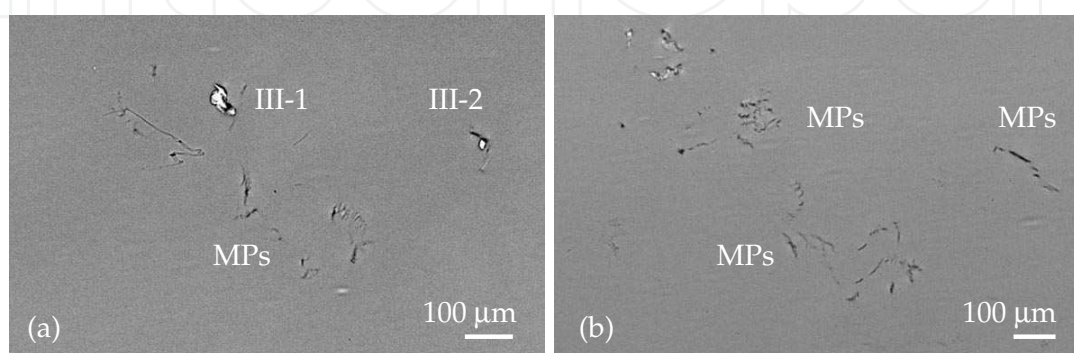

Figure 5. Pores and MPs in the wafers III, IV. The pores are counted III-1 and III-2 (a). MPs in the wafer IV (b).
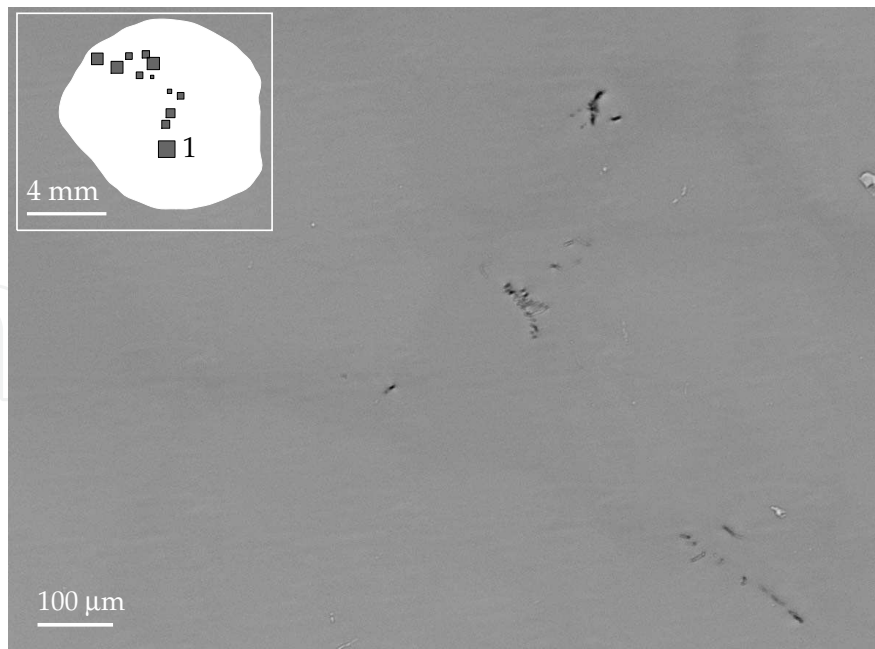
Figure 6. SR phase-contrast image of MPs in the latest-to-grow wafer VI. Schematic of the wafer with black squares highlighting the locations of MPs is shown in the inset. MPs are located on the square #1.

respectively. One can see that the wafer I has higher density of pores. In addition, Figs. 3(a), (b) and (c) taken in SR X-rays and PL, respectively, show pores and FPIs in the wafer I located just outside the scope of the image in Fig. 2(c). The high resolution of Fig. 3(a) demonstrates that the groups of pores (marked by black and white arrows) consist of short tube-shaped or slit-like segments. The morphology of such pores was investigated and attributed to the elastic interaction between MPs and boundaries of FPIs, resulting in coalescence of MPs into larger pores elongated along the boundaries [11, 13]. FPIs were indeed observed on the same location, as revealed by the yellow PL images [28] of n-type 4H-SiC containing N and B in Fig. 3(b) and (c), recorded at 77 K. The comparison with the pore images in the optical micrographs taken prior to the excitation of PL (data not shown), indicates that the pores trace the FPI boundaries.

A group of pores in Fig. 3(a) is partly displayed in the phase contrast image of Fig. 4. One pore from the group is marked by the arrow 2. Notice that the arrow 1 points to the group of MPs located at the place of interest in Fig. 2(c). The magnified image of the group is shown in the inset to Fig. 4. MPs appear as line segments, of which lengths are dependent on the wafer thickness, the miscut angle, and the sample tilting relative to the beam. The MPs run in different directions instead of lying parallel to the growth direction, similar to the observation described in an earlier paper [32]. In fact, the majority of MPs deviated from the growth direction and inclined toward one another or other defects in all six wafers studied.

Interestingly, one can see that the sign of contrast changes per every MP as well as along its axis. For instance, a typical MP image with black edges and a white inside shows a reversal to light edges and a black inside, as is the case in the upper right corner of the inset of Fig. 4. The MP #3 from the group of three MPs and the MP #4 nearby demonstrate the features of black contrast. The effect was well explained by the simulation of MP images measured in a white SR beam [20]. At high angles between the MP axis and the beam, the section size of MP along the beam is small. At low angles, the section size increases, and the wave field

intensity inside the MP starts oscillating. The black contrast appears as a result of average, because in the white radiation fringes are not resolved. In such a way, the image simulation confirms that MPs can move parallel to the growth front towards one another and other defects.

A detailed investigation of MPs shows that the MP #3 and, especially, the MP #4 sharply inclined toward the slit-shaped pores nearby (for instance, to the pore #5 in the inset to Fig. 4). The attraction of the MPs to the pores is confirmed by their contrast behavior and verified by observing the density change of MPs during the SiC growth. The MP density in the group 1 reduced in the wafer II compared to I. The attraction of the MPs to the pore was suggested and explained by their absorption to pores [11, 13]. We believe that, at the initial stage of growth, the pores are generated by the attraction of MPs by FPIs, followed by MP coalescence [10, 11].

The number of pores reduced during the growth, as shown in Fig. 2(c) and (d). Fourteen pores, labeled in the sequence from I-1 to I-14, are identified from the wafer I as shown in Fig. 2(c). They reduce to ten pores on the same location of the wafer II, as shown in Fig. 2(d). We note that pores migrate and noticeably change their configuration. With further growth, the number of pores much more reduces from ten pores in the wafer II to two pores [III-1 and III-2 in Fig. 5(a)] in the wafer III. It is worth noting that new MPs appear in the wafer III. As the growth proceeds, pores are overgrown: no pores detected in the wafer I are seen in the place of interest of wafer IV [Fig. 5(b)]. However, one sees more MPs which obviously group together. They are bent and irregular in shape, size and propagation direction. In the last wafer VI, MPs density remains very inhomogeneous: it is high in some local places, as highlighted in the inset to Fig. 6 by black squares, but low on average. Phase-contrast image of the figure shows the distribution of MPs in a representative location #1. One can see short projection lengths of the MPs running in various directions inside the sample fixed perpendicular to the beam. The imaged area in Fig. 6 is 1.2 mm × 1.2 mm. Taking into account that the area displayed in Fig. 5(b) is slightly smaller (1.2 mm × 0.8 mm), and the number of MPs is noticeably bigger, one can conclude that the density of MPs decreases with growth.

The observations of MPs in this 6*H*-SiC boule and many other similar 6*H* and 4*H*-SiC boules provided strong evidences for the reactions of MPs [7–9]. Reaction between MPs is always a positive process in view of their elimination during the crystal growth.

4. Reduction of micropipes density via self-reactions

4.1. Radii reduction and gradual healing

4.1.1. Micropipe ramification at the front of a growing crystal

Ramification of MPs is accompanied by the partitioning of their Burgers vectors. According to the Frank rule [6], the equilibrium MP radius is proportional to the squared magnitude of its Burgers vector. As a result, ramification of MPs results in a decrease of their radii. The sketch of Fig. 7(a) represents a dislocated MP with the radius r_0 and the Burgers vector b_0 splitted into two smaller ones with the radii and the Burgers vectors r_1, r_2 and b_1, b_2, respectively. A typical phase-contrast image of a ramified dislocation with a hollow core is shown in Fig. 7(b).

The ramification was modeled by Gutkin *et al.* to determine when a MP is favorable to split into a pair of MPs with smaller radii and Burgers vectors [7]. The angle between ramifying segments of the MP 'tree' was assumed to be small enough to consider these segments as a pair of parallel MPs. Also, it was assumed that the ramification required the repulsion of the ramifying segments. It is worth noting that the reverse process of the MP merging may follow the MP split. If the MPs formed by the split stay in contact, they are energetically favored to coalesce and produce a single MP. In this case, the split and following coalescence results only in a decrease in the MP radius. However the merging of the MP segments generated by the split does not occur if these segments, once formed, repulse each other. It was shown that the MPs may either repulse at any distance or repulse at distances d greater than the critical distance d_c and attract each other at $d < d_c$. The ramification of the MP segments (not followed by their coalescence) is possible if they repulse at any distance or the critical distance d_c is small enough. The parameter region where the ramifying MP segments repulse at any distance is shown in Fig. 7(c). The system state diagram is depicted in the coordinate space $(b_1/b_2, r_1/r_2)$. The upper and lower curves separate regions I and III, where the MPs attract each other at short distances while they repel each other at long distances, and the corresponding critical distance $h_c = d_c - r_1 - r_2$ between the MP free surfaces exists, from region II, where the MPs repulse at any distance. As is seen, an attraction area may exist for two same-sign MPs if b_1/b_2 and r_1/r_2 differ by more than 15%–25%. Ramification which does not require overcoming an energetic barrier is possible if the MPs are of the same sign, the radius of the original MP exceeds the equilibrium one, the total MP surface area reduces due to the ramification, and the radii of the ramifying MPs are approximately in the same ratio as the magnitudes of their dislocation Burgers vectors.

4.1.2. Merging of micropipes

Many morphologies of coalesced MPs were observed experimentally in SiC crystals by means of x-ray phase-contrast imaging. To explain these phenomena, a computer simulation of MP evolution was performed [9]. It has been shown that the reaction of MP coalescence gives rise to the generation of new MPs with smaller diameters and Burgers vectors, which again
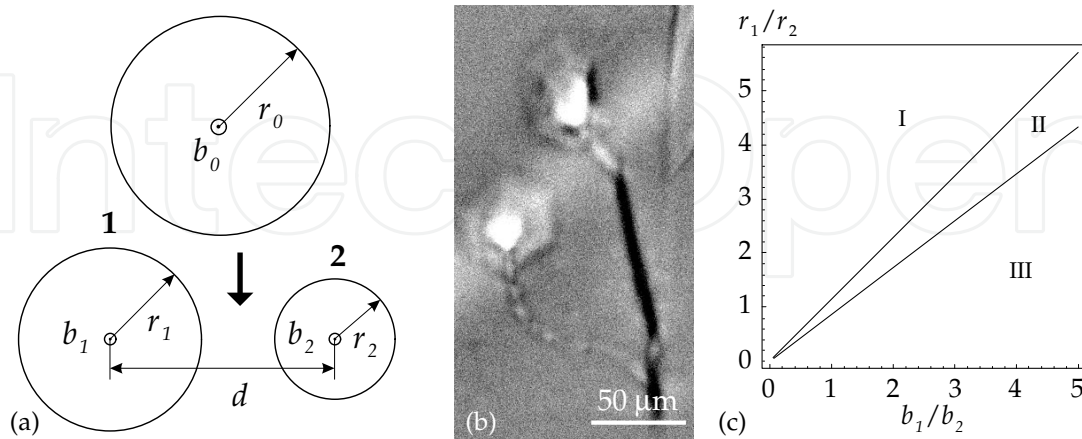

Figure 7. (a) Initial MP with the radius r_0 and the Burgers vector b_0 splits into two parallel dislocated MPs 1 and 2 with the radii and the Burgers vectors r_1, r_2 and b_1, b_2, respectively located at a distance d from each other. (b) SR phase-contrast image of a ramified configuration. Halos correspond to etch pits on the wafer surface. (c) The system state diagram in the coordinate space $(b_1/b_2, r_1/r_2)$. The curves separate parameter regions I and III, where both attraction area and unstable equilibrium position exist for two MPs, from parameter region II, where the MPs repulse at any distance.

leads to diminishing their average density. In particular, when the interacting pair of MPs has incomparable diameters or is located far (at the distance of more than about 5 average MP diameters) from other MPs, the coalescing MPs come directly to each other along the shortest way between them. In this case their behavior is governed by elastic interaction between them only. In some other cases, the ends of two MPs with opposite-sign Burgers vectors start to move around one another. One of the reasons for this is the action of neighboring MPs. The winding of MPs around each other results in coalescence of their subsurface segments. The examples of twisted configurations and the modeling can be found in a review [14].

4.1.3. Correlated reduction in micropipe cross sections

Reactions of ramification, merging and twisting of MPs occur when MPs come in contact, touching each other by their surfaces. However, phase-contrast imaging shows that MPs which are not in a direct contact may have variable cross-sections. In our paper [12], we demonstrated the experimental evidence of two neighboring MPs reducing their diameters (approximately by half) one after another, at different distances from the surface of a grown crystal. This can be treated as an indirect proof of the contact-free reaction. Such an idea appeared when we studied the axial-cut slice of $4H$-SiC boule with the orientation $(\bar{1}1.0)$. MPs located almost parallel to the growth axis were nearly parallel to the sample surface. The sample was fixed on the holder with its surface perpendicular to the beam and rotated to achieve a horizontal position of MP axes. So the images were measured by using the more coherent vertical projection of the source. In the topography mode, the sample was tuned to obtain a symmetrical Laue pattern. An example of an indexed Laue pattern for the $(\bar{1}1.0)$ sample orientation is displayed in Fig. 8(a). One can see many diffraction vectors **g** available for the characterization of dislocations.

For few individual MPs, the distances between the edges modified along their axes showing that their cross-sections changed through the crystal. A good example is the MP pair shown in Fig. 8(b) and (c). An optical micrograph of Fig. 8(c) displays vertical lines of black contrast which are non-uniformly distributed over the sample area and uneven horizontal lines of light contrast. The former are attributed to MPs and the latter to layered inclusions of foreign polytypes ($6H$ and $15R$). We note that MPs agglomerate along the boundaries of the inclusions. The group of closely spaced MPs labeled as MP1 and MP2 is located distant from the other MPs. This particular group was examined in detail in synchrotron light. To indicate the positions of the MPs in figures 8 and 9, we used the features of non-variable contrast, namely, the morphological defect [visible in Fig. 8(c) to the left from the MP1] and the MP bundle located at a distance of 950 μm and 1100 μm, respectively.

Fig. 9(a) and (b) demonstrate X-ray topographs of the MPs recorded in the $\bar{2}1.\bar{2}$ and $01.\bar{1}0$ reflections, respectively. The white arrow indicates the MP1 located at a distance of 950 μm from the mark (that is the morphological defect) shown in Fig. 8(c). The diagram in Fig. 9(c) represents the diffraction geometry. Synchrotron beam propagates along the surface normal $[\bar{1}1.0]$, while the basal plane normal $[00.1]$ lies perpendicular to the beam. We suspect that the dislocation Burgers vector **b** of the MP1 is parallel to $[00.1]$. The diffraction vectors $\mathbf{g}_1 = \bar{2}1.\bar{2}$, and $\mathbf{g}_2 = 01.\bar{1}0$ and the Burgers vector $\mathbf{b}\parallel [00.1]$ are projected onto the film. The angles between the projections, $\angle\mathbf{g}_1$, **b** and $\angle\mathbf{g}_2$, **b**, are also displayed. We note that, for a pure screw dislocation, its image is invisible when $\mathbf{g} \cdot \mathbf{b} = 0$. In Fig. 9 one notices that the contrast increases with the decrease of the angle. The MP1 is invisible in the $\bar{2}1.\bar{2}$ topograph when $\angle\mathbf{g}_1$, **b** = 78.8°, as in Fig. 9(a), but discernible in the $01.\bar{1}0$ reflection when $\angle\mathbf{g}_2$, **b** = 20.6°, as in Fig. 9(b). The contrast behavior indicates that the dislocation of the MP1 is of screw type.
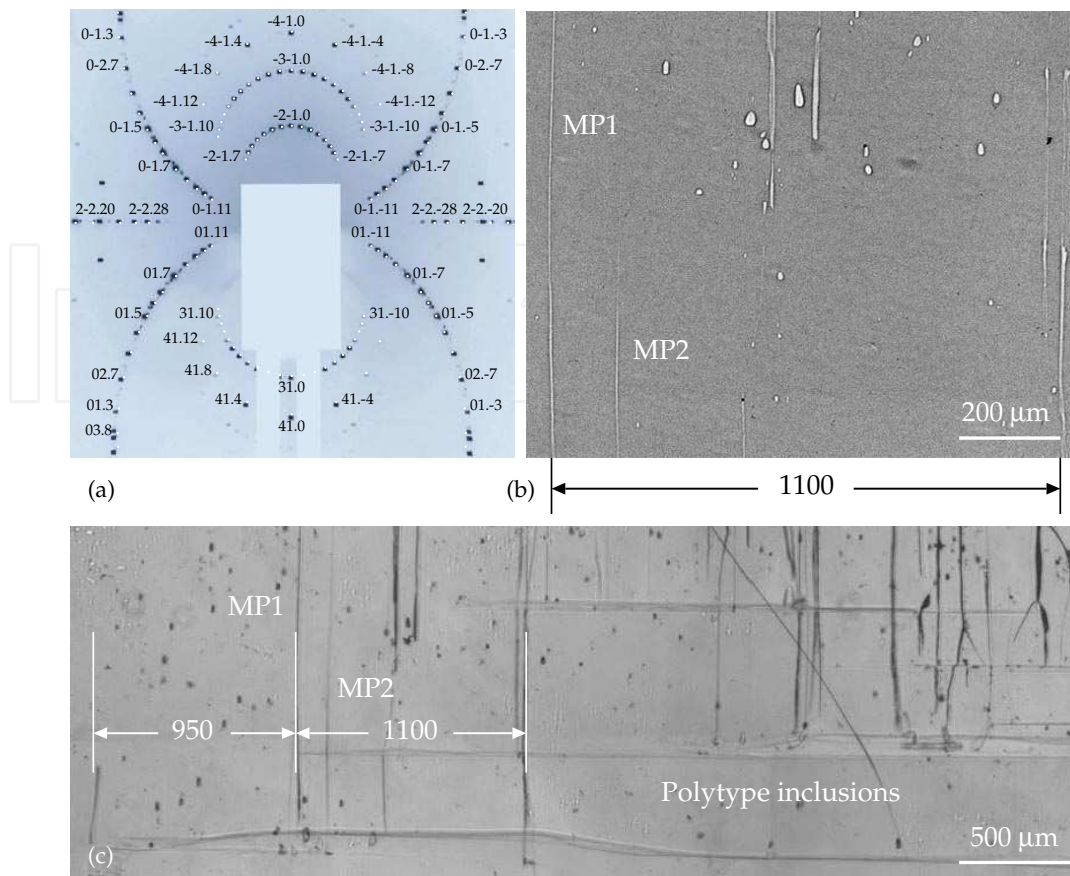
Figure 8. (a) Indexed Laue pattern for ($\overline{1}$1.0) 4*H*-SiC wafer (direction [00.1] horizontal) fixed perpendicular to SR beam. The sample-to-film distance is 130 mm. (b) SR phase-contrast image of the studied MPs, MP1 and MP2. (c) Optical micrograph (transmission) of MPs and foreign polytype inclusions. The distances from MP1 to the morphological defect (950) and the MPs bundle (1100) are shown in microns.

Phase contrast images of the MPs 1 and 2 were measured in a series at the distances from 5 to 45 cm from the sample to detector, increasing the distance every 5 cm. The image registered at the distance of 10 cm is shown in Fig. 10(a). To determine the characteristic sizes of the MP cross sections in different points along the MP axis, we applied the method of computer simulation [1, 19] of the measured intensity profiles. For every MP cross section under investigation, the computer program calculated many profiles for various possible section sizes on the base of Kirchhoff propagation to find the profile, which gives the best fit to the experimental profile. The parameters could be varied by user as well as via automatic procedures. One procedure calculated all points over a square net, while the other one looked for the best fit at every step and arrived at the best matching point. The coincidence allowed us to determine both the longitudinal (along the beam) and transverse (across the beam) sizes of the section [Fig. 10(b)].

The transverse diameters of MP1 and MP2 are presented in Fig. 10(a) versus the distance along the pipe axes increasing in the growth direction. It is seen that the transverse size of MP1 reduces from 7.4 to 2.1 μm with growth. At the same time, the transverse size of the MP2 reduces from 4.1 to 1.6 μm. In contrast, the longitudinal diameters remain almost the same as of the order of 0.8 μm for the MP1 and 0.5 μm for the MP2 (data not shown). In the correlated decrease of the MP1 and MP2 cross-section sizes in Fig. 10(a), several features are apparent. A remarkable decrease in the MP1 cross-section size occurs in the distance
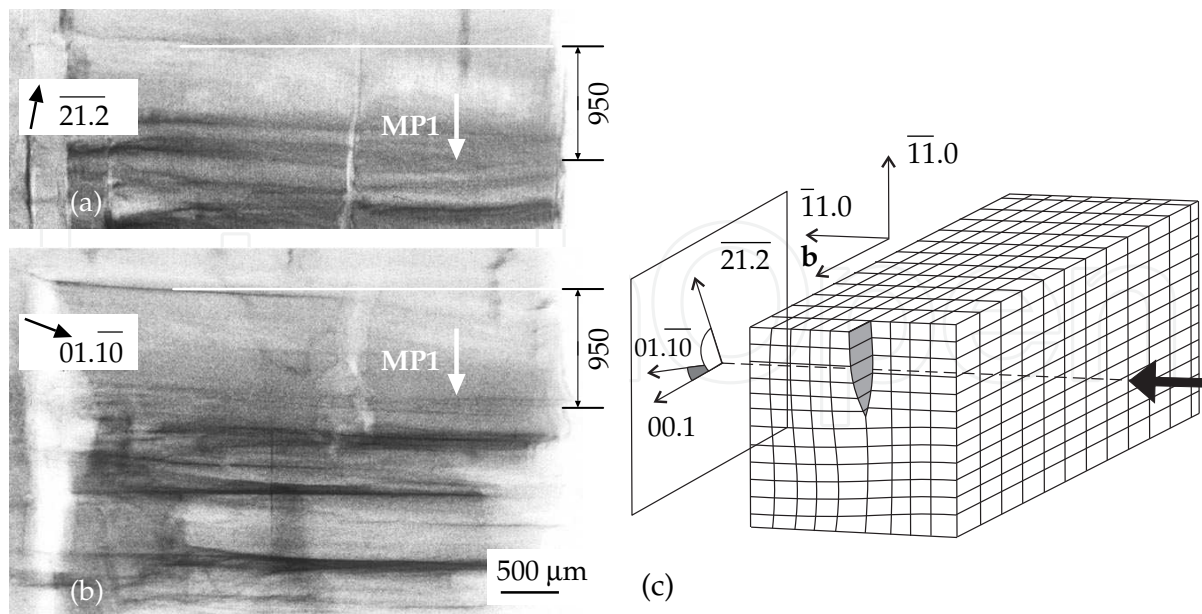
Figure 9. SR white beam topographs of MP1 and adjacent MPs obtained in the reflections $\mathbf{g}_1 = \overline{21}.\overline{2}$ (a) and $\mathbf{g}_2 = 01.\overline{10}$ (b). The position of MP1 is determined relative to the morphological defect shown in Fig. 8. Schematic diagram of the diffraction geometry (c). SR beam (a black arrow) propagates parallel to $[\overline{1}1.0]$. The dislocation Burgers vector $\mathbf{b}$ of MP1 is supposed parallel to $[00.1]$, and the angles are $\angle\mathbf{g}_1, \mathbf{b} = 78.8°$ and $\angle\mathbf{g}_2, \mathbf{b} = 20.6°$.
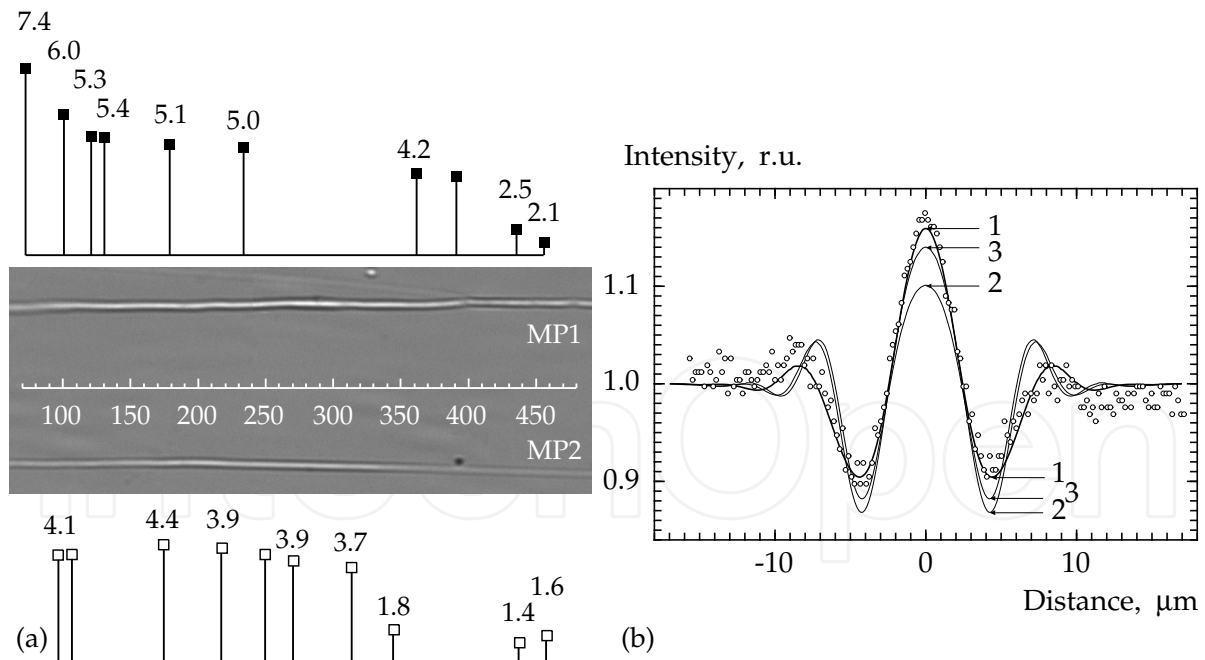

Figure 10. (a) Phase contrast image of micropipes MP1 and MP2 in the interval of 70–500 μm along the pipe axes. The sample-to-detector distance is 10 cm. Variation in transverse cross-section sizes along the lines of MP1 (black squares) and MP2 (open squares) are shown in μm. (b) The experimental (open circles) and simulated (curves 1–3) intensity profiles (the intensity in relative units via the distance across the MP image). The best agreement is achieved through a sequential adjustment in the pipe diameters perpendicular and parallel to the beam. The sample-scintillator distance is 45 cm. The transverse/longitudinal diameters are equal to 5.6/1.0 μm (curve 1, fit = 1.92×10^{-4}). For comparison, curve 2 shows the best fit (8.12×10^{-4}) for the circular cross section 1.76/1.76 μm, while curve 3 is given for the intermediate case 3.0/1.4 μm (fit = 5.71×10^{-4}).

interval from 74 to 132 μm while the transverse diameter of MP2 drastically decreases later in the distance interval from 314 to 345 μm. In addition, a rapid decrease of the transverse diameter of MP1 happens in the distance interval from 393 to 458 μm when the transverse diameter of MP2 remains almost invariable.

The radii reduction of both MPs was explained by a contact-free reaction between them [12, 14]. We suppose that the MP1 and MP2 contain superscrew dislocations with opposite Burgers vectors $\mathbf{b}_1$ and $\mathbf{b}_2$. In case of a contact-free interaction micropipe MP1 emits a full-core dislocation half-loop, which expands by gliding, reaches the surface of micropipe MP2, and reacts with its dislocation. The corresponding dislocation reactions are described by equations: $\mathbf{b}_1 - \mathbf{b}_0 = \mathbf{b}_3$ and $\mathbf{b}_2 + \mathbf{b}_0 = \mathbf{b}_4$, where $\mathbf{b}_3$ and $\mathbf{b}_4$ are new Burgers vectors of micropipes MP1 and MP2, respectively. Strong reduction in the radii can lead to their gradual healing.

4.2. Annihilation of micropipes

MP merging may lead to the annihilation of initial MPs at the growing surface. We considered the motion of subsurface segments of MPs under the action of elastic forces due to their interaction and some effective friction [9]. The latter accounted for some extra surface energy related to the steps appearing on the pipe cylindrical surfaces during lateral displacements of the pipe segments. As a result, various reactions between the subsurface pipe segments were observed. In particular, it has been shown that the reaction of MP coalescence can lead to the annihilation of initial MPs. Some typical defect configurations in a 3D space are displayed in Fig. 11. They may be subdivided into planar and twisted pipe configurations. The planar configurations arise when the interacting pair of MPs is located far from other MPs; and the coalescing MPs come to each other along the shortest way [Fig 11(a)]. The twisted configurations like double spirals form if the interacting MPs are located within dense groups of other MPs. In this case, the coalescing MPs twist [Fig 11(b)]. When the magnitudes of Burgers vectors are the same, the initial defect configuration of a dipole is transformed into a new configuration of a semiloop [Fig. 11(c)]. As a result, we expect that the density of MPs would diminish during the crystal growth. The smaller the surface energy is the faster this process would be.

5. Structural models of pore overgrowth

5.1. Generation of pores in early stage of SiC growth

From our observations of FPIs, pores, MPs and their changes during the bulk SiC crystal growth described above, we suggest the formation mechanisms of defects as follows. The nucleation of FPIs in the initial stage is suggested as a basis of massive generation of full-core dislocations [26], pores and MPs [10, 11, 13, 31]. The bottom and lateral faces of growing FPIs are possibly the formation sites of interface dislocation structures to accommodate the misfit or misorientation of the matrix and FPI's crystalline lattices. The FPI boundaries are also able to serve as easy paths and sinks for vacancies which are nucleated at the growth front and migrate towards the crystal bulk. High densities of interface dislocations and vacancies thus formed possibly lead to coagulation of vacancies, forming slit-like pores along the FPI boundaries.
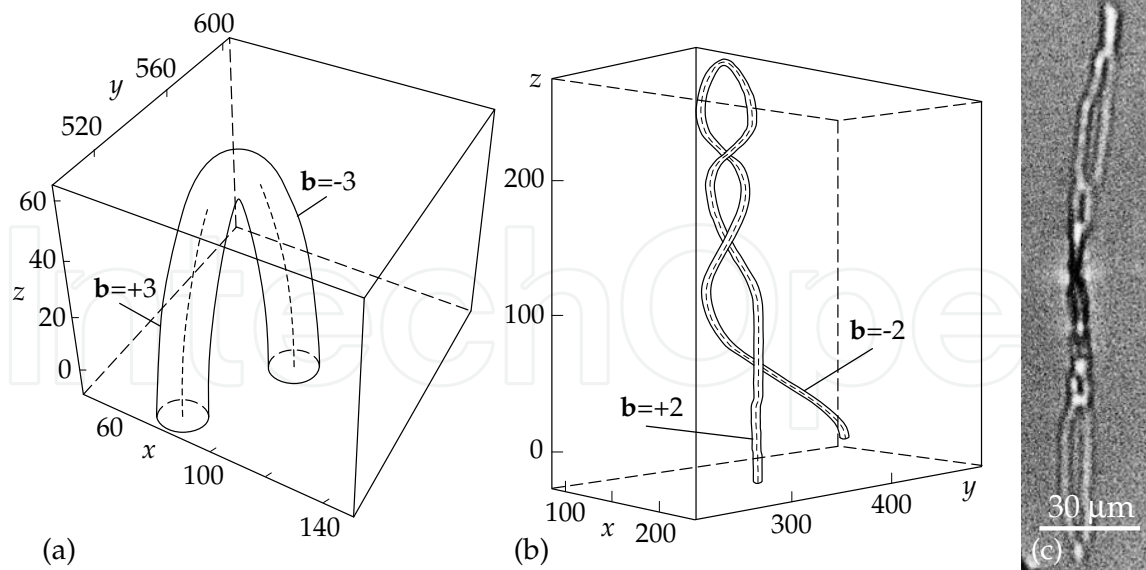
Figure 11. Coalescence of MPs with equal magnitudes of Burgers vectors results in the annihilation of the subsurface MP segments (a, b). The coalescing MPs come to each other along the shortest way (a) or twist (b). The Burgers vectors are shown in units of c, which is the lattice parameter in the growth direction. The coordinates x and y are given in units of $Gc^2/(8\pi^2\gamma)$, where G is the shear modulus and γ is the specific surface energy. The length of MPs (along the z axes) is in arbitrary units that depend on the growth rate. SR phase-contrast image of semi-loops resulting from macropipes twisting (c).

Another possible mechanism of pore formation is the attraction and agglomeration of MPs at FPI boundaries [10, 11, 13], for instance, resulting in the majority of pores observed at the boundaries of FPIs (Fig. 3). By effectively accommodating both the dilatation and orientation misfits between FPI and matrix, these pores in early stages can attract additional random full-core dislocations and MPs from neighboring regions (Fig. 4), as earlier described in detail [13]. In such a way, the interface pores can extend along FPI boundaries and accumulate dislocation charge that is the resulting Burgers vector of all the dislocations absorbed by the pore. Of course, one can not exclude the presence of the pores that have been formed by the other mechanisms and do not contain any dislocation charge.

5.2. Generation of MPs in the intermediate stage

When the FPIs stop to grow and become overgrown by the matrix, there is no reason for the pore formation as misfit defects. The disappearance of pores started to occur at this point, as seen in Figs. 2 and 5. We suggest three possible mechanisms that can explain the disappearance and its contribution to the increase in MP density.

a First, pores can dissolve through emission of vacancies, which migrate to full-core threading dislocations on the FPI/matrix interface [15, 26] and are absorbed by them, as illustrated in Fig. 12. These dislocations can reach the growth front and proceed to grow with it [Fig. 12(a)]. At the dislocation core, these vacancies are coagulated with the vacancies that migrate from the growth front along the dislocation cores, thus forming embryos of new MPs [Fig. 12(b)].

b Second, the pores can be overgrown by the lateral growth of the crystal and, if they contain dislocations with large Burgers vectors, can transform to MPs by the mechanism described earlier [21].
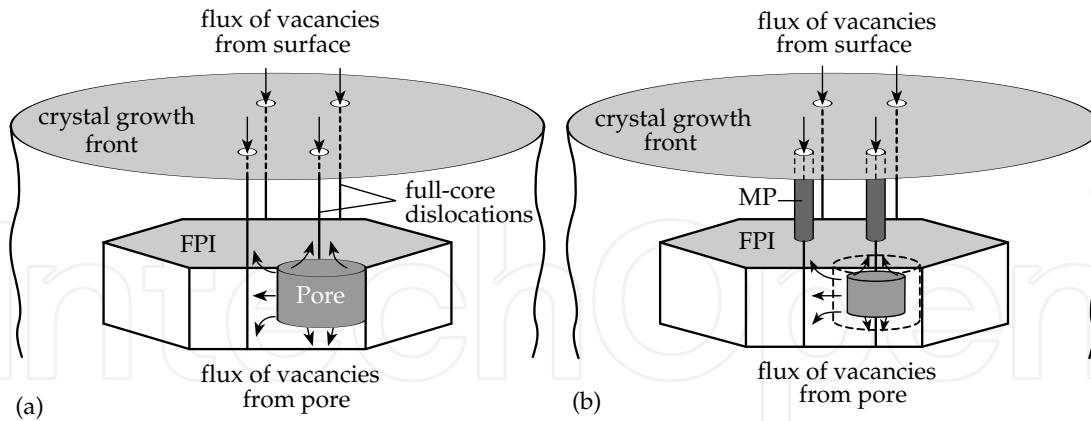
Figure 12. Mechanism of MP nucleation through coagulation of vacancies at the cores of threading dislocations. (a) Pore at the boundary of FPI starts to dissolve by emitting vacancies which migrate to neighboring full-core threading dislocations. (b) Vacancies from pore and growth surface migrate along the dislocation cores, meet and coagulate, thus transforming full-core dislocations to MPs.
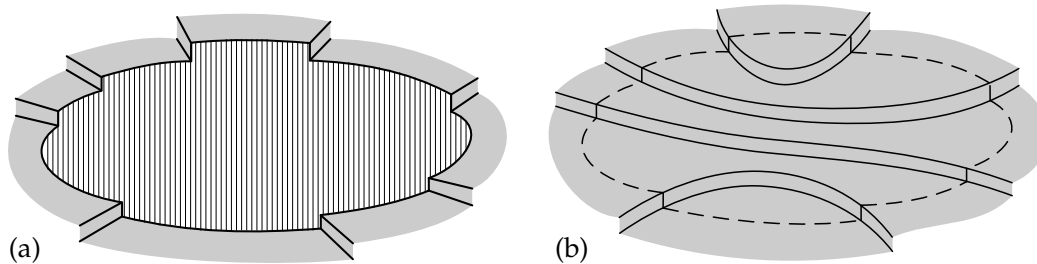

Figure 13. The pore of a convex shape has equal number of up-steps and down-steps and does not contain screw dislocation. (a) Open pore, (b) overgrown pore.

  c Third, if pores have complex shapes (like those represented in Figs. 2–4, they can produce dislocated MPs during their lateral overgrowth even without full-core dislocations as described below.

The surface regions around pores always contain surface steps. If the numbers of the steps up and down (let us call them up-steps and down-steps, respectively) are equal, there would be no screw dislocation inside the pore. Otherwise there should be a screw dislocation with a Burgers vector of the magnitude equal to the difference between the sum heights of up-steps and down-steps. Let us consider the first case as shown schematically in Fig. 13 and Fig. 14 for simple convex and complex pore shapes, respectively. If the pore shape is convex (say, circular or elliptical), its overgrowth can hardly lead to the formation of screw dislocations (Fig. 13). However, if the pore shape is complex with some concave fragments [Fig. 14(a)], one can expect that the pore starts to overgrow through a bridge between two opposite concave fragments in a narrow part of the pore [Figs. 14(b) or (c)]. This bridge can separate the initial pore into smaller ones. If the two new pores have different numbers of up-steps and down-steps on the growth surface, the difference can be compensated by large (or small) steps on the bridge [it is called S-bridge here, Fig. 14(b)] with no screw dislocations. Otherwise the bridge can have a smooth surface without steps and be distorted [it is called D-bridge here, Fig. 14(c)], forming a semi-loop of superdislocation. The edge segment of the semi-loop lies under the D-bridge, while the two screw segments are within their new pores.
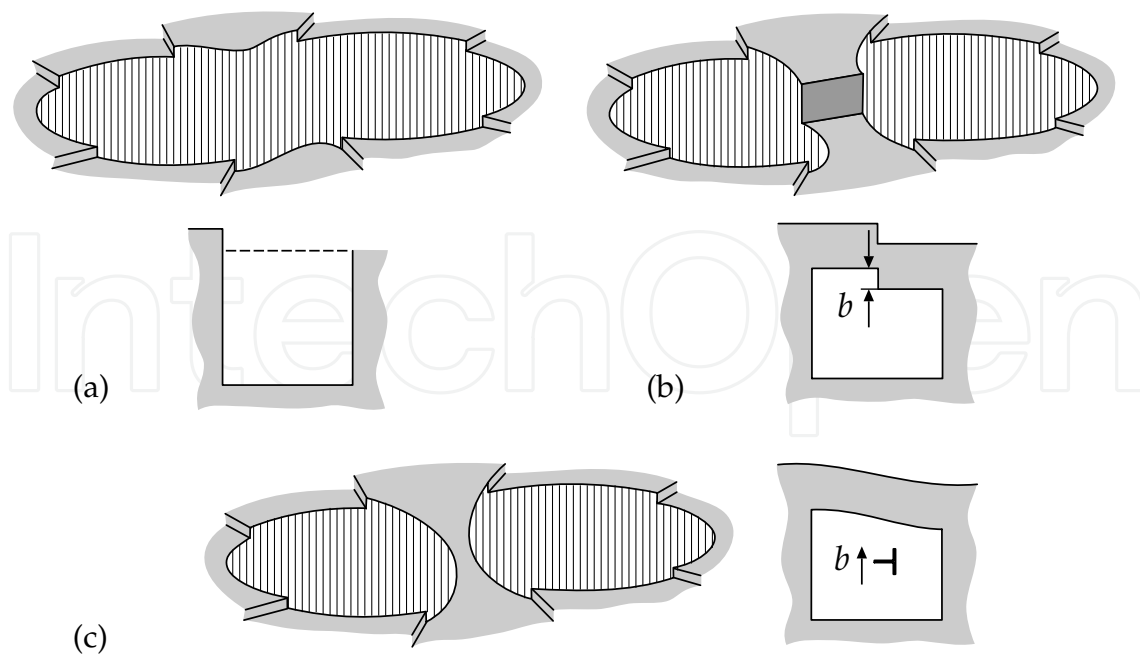
Figure 14. (a) The pore of a complex shape has equal number of up-steps and down-steps and first does not contain screw dislocation. (b) Pore overgrowth starts with a stepped bridge (S-bridge); if the large step compensates small steps around the two new pores, then no screw dislocations appear. (c) Pore overgrowth starts with a distorted bridge (D-bridge); there is no compensation of small steps around the two new pores, in which case a dislocation semi-loop arises: the edge segment of the semi-loop lies under the D-bridge, while two screw segments are within their new pores. These new pores become embryos of dislocated MPs.

These new pores can become embryos of dislocated MPs. It is worth noting that a similar mechanism for screw dislocation nucleation at foreign phase inclusions was first proposed by Chernov [4]. Dudley *et al.* experimentally observed and explained the nucleation of a pair of MPs at an inclusion in 4*H*-SiC [5]. In such a way, a pore elongated along the growth front and overgrown with the formation of many D-bridges can 'produce' many MPs of alternate dislocation signs of equal or different radii depending on the dislocation Burgers vectors. Similar separate dense arrays of MPs are demonstrated in Figs. 5 and 6.

As a result, the density of pores (and full-core dislocations) decreases at this stage of crystal growth, while the density of MPs increases, as seen in Fig. 5.

5.3. Evolution of defects in later stage

The situation at the next stage of the crystal growth depends on whether new FPIs are generated or not. If generated, then the stages described above are repeated. However, though formed as explained in the intermediate stage, MPs can be attracted to FPIs and absorbed by their boundaries, producing extended pores there by agglomeration [10, 11]. If new FPIs are not nucleated, the processes of self-organization occur in the MPs ensemble: MPs elastically interact and react with each other as well as with full-core dislocations, as described in the section 4. As a result, some MPs annihilate or diminish their Burgers vectors and are finally healed. Otherwise they form separate dense groups of MPs which proceed to grow with the crystal.

6. Conclusions

The evolution of defects was investigated by using on-axis and axial-cut slices prepared from 6*H* and 4*H*-SiC PVT grown crystals. SR phase contrast imaging enabled us to visualize not only MPs and the pores formed at the boundaries of FPIs, but also their changes during SiC growth. Detailed mechanisms for the evolution from FPIs to pores and finally to MPs were suggested. In the early growth stage, FPIs not only induce massive generation of full-core dislocations and MPs but also attract them, forming slit-type pores at the boundaries of FPIs. In the intermediate stage, when FPIs stop to grow and become overgrown by the matrix, the pore density significantly reduces, which is attributed to their transformation into new MPs. In the later stage, the MP density decreases, providing evidence for their partial annihilation and healing.

The reactions of MPs in view of their elimination during the crystal growth were briefly reviewed. The reduction of MP cross-section, which can eventually results in its overgrowth, occurs at the crystal growth when MP splits, as well as merges or interacts with another MP in a non-contact mode. The split happens if the splitting dislocation overcomes the MP attraction zone and the flat crystal surface attraction zone. Merging can occur due to collective mesoscopic effects in a random ensemble of MPs. The twisted dipoles result under the action of neighboring MPs. When the magnitudes of Burgers vectors are the same, the dipole is transformed into a new configuration of a semiloop. Such reactions of ramification and coalescence of MPs, as well as annihilation for dipoles of MPs, were observed by phase-contrast imaging. Computer simulation of phase-contrast images demonstrated the correlated reduction in the radii of two remote MPs, which provided a support of contact-free reaction between them.

This study suggests that the key point for the elimination of defects from such crystals is the suppression of FPI nucleation. The reactions of MPs are necessary for diminishing their density; and such reactions should be faster as the surface energy becomes smaller.

Author details

T. S. Argunova[1,2], M. Yu. Gutkin[3,4,5],
J. H. Je[2,*], V. G. Kohn[6] and E. N. Mokhov[1]

[1]Ioffe Physical-Technical Institute, RAS, St. Petersburg, Russia
[2]X-ray Imaging Center, Department of Materials Science and Engineering, Pohang University of Science and Technology, Pohang, Republic of Korea
[3]Institute of Problems in Mechanical Engineering, RAS, St. Petersburg, Russia
[4]Department of Physics of Materials Strength and Plasticity, St. Petersburg State Polytechnical University, St. Petersburg, Russia
[5]Department of Theory of Elasticity, St. Petersburg State University, St. Petersburg, Russia
[6]Russian Research Center 'Kurchatov Institute', Moscow, Russia

References

[1] Argunova, T.; Kohn, V.; Jung, J-W.; Je J-H. (2009). Elliptical micropipes in SiC revealed by computer simulating phase contrast images. *Phys. Status Solidi* A, Vol. 206, 1833–1837.

[2] Baik, S.; Kim, H. S.; Jeong, M. H.; Lee, C. S.; Je, J. H.; Hwu, Y.; Margaritondo, G. (2004). International consortium on phase contrast imaging and radiology beamline at the Pohang Light Source. *Rev. Sci. Instrum.*, Vol. 75, 4355–4358.

[3] Chen, Yi; Dudley, M.; Sanchez, E.; Macmillan, M. (2008). Simulation of grazing-incidence synchrotron white beam X-ray topographic images of micropipes in 4*H*-SiC and determination of their dislocation senses. *J. Electron. Mater.*, Vol. 37, 713–720.

[4] Chernov, A. A. (1989). Formation of crystals in solutions. *Contemp. Phys.*, Vol. 30, 251-276.

[5] Dudley, M.; Huang, X. R.; Huang, W.; Powell, A.; Wang, S.; Neudeck, P.; Skowronski, M. (1999). The mechanism of micropipe nucleation at inclusions in silicon carbide. *Appl. Phys. Lett.*, Vol. 75, 784–786.

[6] Frank, F. C. (1951). Capillary equilibria of dislocated crystals. *Acta Crystallogr.*, Vol. 4, 497–501.

[7] Gutkin, M. Yu.; Sheinerman, A. G.; Argunova, T. S.; Je, J. H.; Kang, H. S.; Hwu, Y.; Tsai W-L. (2002). Ramification of micropipes in SiC crystals. *J. Appl. Phys.*, Vol. 92, 889–894.

[8] Gutkin, M. Yu.; Sheinerman, A. G.; Argunova, T. S.; Mokhov, E. N.; Je, J. H.; Hwu Y.; Tsai W-L.; Margaritondo G. (2003). Micropipe evolution in silicon carbide. *Appl. Phys. Lett.*, Vol. 83, 2157–2159.

[9] Gutkin, M. Yu.; Sheinerman, A. G.; Argunova, T. S.; Mokhov, E. N.; Je, J. H.; Hwu Y.; Tsai W-L.; Margaritondo G. (2003a). Synchrotron radiographic study and computer simulation of reactions between micropipes in silicon carbide. *J. Appl. Phys.*, Vol. 94, 7076–7082.

[10] Gutkin, M. Yu.; Sheinerman, A. G.; Argunova, T. S.; Yi, J.-M.; Kim, M.-U.; Je, J.-H.; Nagalyuk, S. S.; Mokhov, E. N.; Margaritondo, G.; Hwu, Y. (2006). Interaction of micropipes with foreign polytype inclusions in SiC. *J. Appl. Phys.*, Vol. 100, 093518.

[11] Gutkin, M. Yu.; Sheinerman, A. G.; Argunova, T. S.; Yi, J.-M.; Je, J.-H.; Nagalyuk, S. S.; Mokhov, E. N.; Margaritondo, G.; Hwu, Y. (2007). Role of micropipes in the formation of pores at foreign polytype boundaries in SiC crystals. *Phys. Rev.* B, Vol. 76, 064117.

[12] Gutkin, M. Yu.; Sheinerman, A. G.; Smirnov, M. A.; Kohn, V. G.; Argunova, T. S.; Je, J. H.; Jung J. W. (2008). Correlated reduction in micropipe cross sections in SiC growth. *Appl. Phys. Lett.*, Vol. 93, 151905.

[13] Gutkin, M. Yu.; Sheinerman, A. G.; Smirnov, M. A.; Argunova, T. S.; Je, J.-H.; Nagalyuk, S. S.; Mokhov, E. N. (2009). Micropipe absorption mechanism of pore growth at foreign polytype boundaries in SiC crystals. *J. Appl. Phys.*, Vol. 106, 123515.

[14] Gutkin, M. Yu.; Argunova, T. S.; Kohn, V. G.; Sheinerman, A. G.; Je, J. H. (2011). Micropipe Reactions in Bulk SiC Growth. *Silicon Carbide,* ISBN 978-953-307-348-4, IN-TECH. URL: *http://www.intechopen.com/articles/show/title/micropipe-reactions-in-bulk-sic-growth*

[15] Ha, S.; Nuhfer, N. T.; Rohrer, G. S.; de Graef, M.; Skowronski, M. (2000). Identification of prismatic slip bands in 4*H*-SiC boules grown by physical vapor transport. *J. Electron. Maters.*, Vol. 29, L5–L8.

[16] Hatakeyama, T.; Ichinoseki, K.; Fukuda, K.; Higuchi, N.; Arai, K. (2008). Evaluation of the quality of commercial silicon carbide wafers by an optical non-destructive inspection technique. *J. Cryst. Growth*, Vol. 310, 988-992.

[17] Huang, X. R.; Dudley, M.; Vetter, W. M.; Huang, W.; Wang, S. (1999). Direct evidence of micropipe-related pure superscrew dislocations in SiC. *Appl. Phys. Lett.*, Vol. 74, No. 3; 353–355.

[18] Kamata I.; Nagano, M.; Tsuchida, H.; Chen, Yi.; Dudley, M. (2009). Investigation of character and spatial distribution of threading edge dislocations in 4*H*-SiC epilayers by high-resolution topography. *J. Cryst. Growth*, Vol. 311, 1416–1422.

[19] Kohn, V. G.; Argunova, T. S.; Je, J. H. (2007). Study of micropipe structure in SiC by x-ray phase contrast imaging. *Appl. Phys. Let.*, Vol. 91, 171901.

[20] Kohn, V. G.; Argunova, T. S.; Je, J. H. (2012). Reason of a contrast change in SR-images of micropipes in SiC. *J. Surf. Investig-X-ra.*, Vol. 10. 60-65.

[21] Kuhr, T.; Sanchez, E.; Skowronski, M.; Vetter, W.; Dudley, M. (2001). Hexagonal voids and the formation of micropipes during SiC sublimation growth. *J. Appl. Phys.*, Vol. 89, 4625–4630.

[22] Lin, Sh.; Chen, Zh.; Yang, Y.; Liu, S.; Ba, Y.; Li L.; Yang, Ch. (2012). Formation and evolution of micropipes in SiC crystals. *CrystEngComm*, Vol. 14, 1588–1594. URL: http://pubs.rsc.org/en/content/articlepdf/2012/ce/c1ce05806a

[23] Liu, J.-L.; Gao, J.-Q.; Cheng, J.-K.; Yang, J.-F.; Qiao, G.-J. (2007). Methods for the reduction of the micropipe density in SiC single crystals. *J. Mater. Sci.*, Vol. 42, 6148–6152.

[24] Nakamura, D.; Yamaguchi, S.; Gunjishima, I.; Hirose, Y.; Kimoto, T. (2007). Topographic study of dislocation structure in hexagonal SiC single crystals with low dislocation density. *J. Cryst. Growth*, Vol. 304, 57–63.

[25] Nakamura, D.; Yamaguchi, S.; Hirose, Y.; Tani, T.; Takatori, K.; Kajiwara, K.; Kimoto, T. (2008). Direct determination of Burgers vector sense and magnitude of elementary dislocations by synchrotron white x-ray topography. *J. Appl. Phys.*, Vol. 103, 013510.

[26] Ohtani, N.; Katsuno, M.; Tsuge, H.; Fujimoto, T.; Nakabayashi, M.; Yashiro, H.; Sawamura, M.; Aigo, T.; Hoshino, T. (2006). Propagation behavior of threading dislocations during physical vapor transport growth of silicon carbide (SiC) single crystals. *J. Cryst. Growth*, Vol. 286, 55–60.

[27] Ohtani, N.; Katsuno, M.; Tsuge, H.; Fujimoto, T.; Nakabayashi, M.; Yashiro, H.; Sawamura, M.; Aigo, T.; Hoshino, T. (2006a). Dislocation processes during SiC bulk crystal growth. *Microelectron. Eng.*, Vol. 83; 142–145.

[28] Saparin G. V., Obyden, S. K.; Ivannikov, P. V.; Shishkin, E. B.; Mokhov, E. N.; Roenkov, A. D.; Hofmann, D. H. (1997). Three-dimensional studies of SiC polytype transformations. *Scanning*, Vol. 19, 269–274.

[29] Schmitt, E.; Straubinger, T.; Rasp, M.; Vogel, M.; Wohlfart, A. (2008). Polytype stability and defects in differently doped bulk SiC. *J. Cryst. Growth*, Vol. 310, 966–970.

[30] Tsuchida, H.; Kamata, I.; Nagano, M. (2007). Investigation of defect formation in 4H-SiC epitaxial growth by X-ray topography and defect selective etching. *J. Cryst. Growth*, Vol. 306, 254–261.

[31] Vodakov, Yu. A.; Roenkov, A. D.; Ramm, M. G.; Mokhov, E. N., Makarov Yu. N. (1997). Use of Ta-container for sublimation growth and doping of SiC bulk crystals and epitaxial layers. *Phys. Stat. Sol.* B, Vol. 202, 177–200.

[32] Wang, Y.; Ali, G.; Mikhov, M.; Vaidyanathan, V.; Skromme, B.; Raghothamachar, B.; Dudley, M. (2005). Correlation between morphological defects, electron beam-induced current imaging, and the electrical properties of 4*H*-SiC Schottky diodes. *J. Appl. Phys.*, Vol. 97, 013540.

[33] Wierzchowski, W.; Wieteska, K.; Balcer, T.; Malinowska, A.; Graeff, W.; Hofman, W. (2007). Observation of individual dislocations in 6H and 4H SiC by means of back-reflection methods of X-ray diffraction topography. *Cryst. Res. Technol.*, Vol. 42, 1359–1363.